Handheld photoacoustic microscopy to detect melanoma depth *in vivo*

Yong Zhou,[1] Wenxin Xing,[1] Konstantin I. Maslov,[1] Lynn A. Cornelius,[2,3] and Lihong V. Wang[1,4]

[1]*Washington University in St. Louis, Department of Biomedical Engineering, Optical Imaging Laboratory, 1 Brookings Drive, Campus Box 1097, St. Louis, Missouri 63130, USA*

[2]*Washington University School of Medicine, Division of Dermatology, 660 S. Euclid, Campus Box 8123, St. Louis, Missouri 63110, USA*

[3]*e-mail: LCORNELI@DOM.wustl.edu*

[4]*e-mail: lhwang@wustl.edu*

We developed handheld photoacoustic microscopy (PAM) to detect melanoma and determine tumor depth in nude mice *in vivo*. Compared to our previous PAM system for melanoma imaging, a new light delivery mechanism is introduced to improve light penetration. We show that melanomas with 4.1 and 3.7 mm thicknesses can be successfully detected in phantom and in *in vivo* experiments, respectively. With its deep melanoma imaging ability and handheld design, this system can be tested for clinical melanoma diagnosis, prognosis, and surgical planning for patients at the bedside.   © 2014 Optical Society of America

OCIS codes: (170.5120) Photoacoustic imaging; (170.3880) Medical and biological imaging; (170.3890) Medical optics instrumentation.

http://dx.doi.org/10.1364/OL.39.004731

Melanoma is a malignant tumor of melanocytes. It is now the fifth most common cancer in the United States [1,2], where there were about 76,690 men and women diagnosed with melanoma in 2013 alone [2,3]. Although melanoma accounts for less than 5% of all skin cancers [2], it causes more than 75% of deaths related to skin cancer [1]. In addition, the incidence of melanoma is increasing faster than that of any other cancer [4]. Consequently, there is an increased demand for accurate diagnosis, prognosis, and treatment of melanoma.

The thickness of a melanoma is a critical parameter for determining definitive treatment and prognosis [5]. Based on its thickness, the tumor (T) classification in the tumor-node-metastasis (TNM) staging system can be further divided into T1 ($\leq$1.0 mm), T2 (1.01–2.0 mm), T3 (2.01–4.0 mm), and T4 (>4.0 mm) [2]. As the thickness increases, so do the chances for developing metastatic disease, and thus, disease mortality. Current diagnoses are dependent upon clinical suspicion, subsequent biopsy, and histologic examination. It has been shown that clinical examination alone may miss certain tumors, and conversely, many benign lesions may be unnecessarily biopsied [6,7]. In trained hands, the use of handheld dermoscopy in the clinic has aided in the diagnosis of melanoma by facilitating the evaluation of surface characteristics of pigmented lesions [8]. It does not, however, enable the determination of tumor thickness and vertical growth of the melanoma, which are important tumor characteristics when it comes to determining surgical treatment. In fact, the surgeon is often met with the confounding situation where a pigmented lesion may be partially biopsied and the diagnosis of melanoma is made. Consequently, the true tumor depth may not be determined because of sampling only part of the tumor, leading to an inaccurate measurement. Thus, a wide local excision (WLE) based upon a provisional tumor depth may not be appropriate, and a second surgery may be required to adequately treat the tumor. Thus, a precise *in vivo* measurement of tumor depth, prior to definitive surgery, would facilitate appropriate patient treatment and help avoid further surgeries.

In the past few years, several noninvasive imaging techniques have been developed for melanoma diagnoses [5,6,9]. However, all of them have limitations. Optical methods, such as dermoscopy [8], total-body photography (TBP) [10], optical coherence tomography [11], scanning confocal microscopy [12], and two-photon microscopy [13], do not have sufficient penetration to determine melanoma depth because they can image only in the ballistic regime. High-frequency ultrasound can provide deeper penetration than optical methods [14]. However, because there is often no sufficient difference in acoustic impedance between melanoma and normal tissues, the image contrast for melanoma is poor. Magnetic resonance imaging (MRI) and positron emission tomography (PET) have also been used in melanoma diagnoses [15,16]. However, they are both expensive and have poor resolution in the skin. Meanwhile, PET has to use tracers for sufficient contrast and can only detect tumors as large as ~1 cm in dimension, which encompasses only a tiny set of T4 primary melanomas and misses all T1–T3 ones.

Recently, photoacoustic microscopy (PAM) has shown strong ability in detecting skin vasculatures with high contrast and deep penetration [17,18]. In PAM, short laser pulses illuminate the object. Following the absorption of photons, ultrasonic waves are induced thermoelastically through the photoacoustic (PA) effect [19,20]. Because melanin in most melanomas has a very broad and strong absorption spectrum, it can be imaged by PAM with high contrast. Meanwhile, because acoustic scattering is low in the tissue, high resolution can be achieved with deep penetration.

Previously, we reported that cutaneous pigmented lesions, melanoma, and the surrounding vasculature could be successfully detected by using dual-wavelength

PAM [21]. In that study, light was transmitted through the whole melanoma, resulting in a high attenuation, with only very few photons reaching the base of the melanoma (true tumor depth). In the end, PA signals were very strong from the surface of the tumor but very weak from the deepest portion. The experimental results showed that a melanoma phantom with a maximum thickness of 1.27 mm could be imaged, which covered only the T1 classification. Using a similar configuration, other studies on melanoma detection can be found elsewhere [22–24]. In this report, we describe a new PAM system with more efficient light illumination. By allowing light to bypass the center of the tumor, more photons reach the inferior depth of the melanoma. Equally important, this system is designed to be handheld, facilitating clinical usage.

Figure 1(a) shows a schematic of the handheld PAM system. A Q-switched pulsed laser (Brilliant B, Quantel, Les Ulis, France) generates light at 532 nm at 10 Hz as the input for the dye cell. The output light of the dye cell is at 650 nm wavelength, where melanoma has high absorption, but both blood and water have low absorption. A lens couples the free-space light into an optical fiber bundle (LightGuideOptics, Rheinbach, Germany), with output fibers arranged in a circle around a focused ultrasonic transducer (IS2502HR, CTS Valpey, Elkhart, Indiana). Compared to our previous PAM system, the light is delivered into the tissue normally instead of obliquely. Thus, the light propagates around the melanoma instead of going through it. Since the surrounding tissue has high optical scattering but low absorption, the light reaching the bottom boundary of the melanoma is increased. The incident beam has an annular shape with 8 mm inner and 20 mm outer diameters. The optical fluence on the skin surface was estimated to be 15 mJ/cm^2, which was less than the safety limit set by the American National Standard Institute (ANSI) (20 mJ/cm^2). The transducer, with 25 MHz central frequency and 100% nominal bandwidth, detects the PA signals. The focal length and diameter of the detector are 12.7 and 6.4 mm, respectively, yielding a numerical aperture (NA) of 0.25. Both the optical fibers and transducer are fixed on a motorized

translation stage [Fig. 1(b)]. Each laser pulse generates a one-dimensional depth-resolved image (A–line). A two-dimensional cross sectional image is acquired by linear scanning of the region of interest. As shown in Figs. 1(a) and 1(b), the motor, translation stage, ultrasonic transducer, and optical fibers are all incorporated in a handheld probe for easy operation. A photograph of the handheld probe is shown in Fig. 1(c).

We use Monte Carlo simulations to show the advantage of the new light illumination mechanism [25]. Figure 2(a) represents the old light illumination mechanism (hereinafter referred to as case 1). The incident angle was set to 45°, which was typical in the previous PAM system. Figure 2(b) shows the new light illumination mechanism (hereinafter referred to as case 2). In both simulations, the same incident energies were used. The same melanoma phantom, with 1 mm thickness and 6 mm diameter, was used in both simulations. The simulation parameters (absorption coefficient of the melanoma phantom, 70 cm^{-1}; absorption coefficient of the background, 0.1 cm^{-1}; scattering coefficients of the melanoma phantom and background, 100 cm^{-1}; scattering anisotropy of the melanoma phantom and background, 0.9) were selected based on normal tissue optical properties at 650 nm wavelength [26,27]. As shown in Fig. 2(c), in case 1, the specific optical absorption (A_e) decreases sharply in the melanoma phantom in the depth direction. However, as shown in Fig. 2(d), in case 2, A_e actually increases in the melanoma phantom in the depth direction. As shown in Figs. 2(a)–2(d), the same black-dashed-square area was chosen to calculate an average A_e at the bottom boundary of the melanoma phantoms for comparison between case 1 and case 2. The average A_e is shown in Fig. 2(e). Although the average A_e at the bottom boundary of the melanoma in the black-dashed-square area was maximized by aligning the light beam in case 1 [shown in Fig. 2(a)], it is still 1660 times weaker than that in case 2. In both thermal and stress
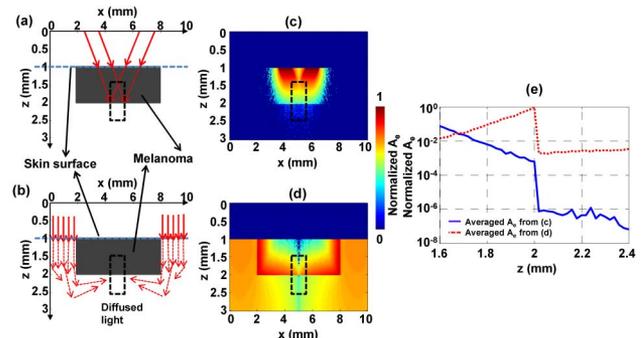
Fig. 2. Monte Carlo simulations of the old and new PAM systems for melanoma imaging. Melanoma phantom and light illumination methods used in the simulations of (a) the old and (b) the new systems. The red arrows show the incident angles and areas of the light used in the Monte Carlo simulations. Specific heat absorption (A_e) distributions in (c) the old and (d) the new PAM systems with the same incident energy. (e) Averaged A_e in the black-dashed-square areas [shown in (a)–(d)] at the bottom boundary of the melanoma phantoms in (c) blue line and (d) red dotted line, showing that the melanoma is much more strongly illuminated at the bottom boundary using the new PAM system.
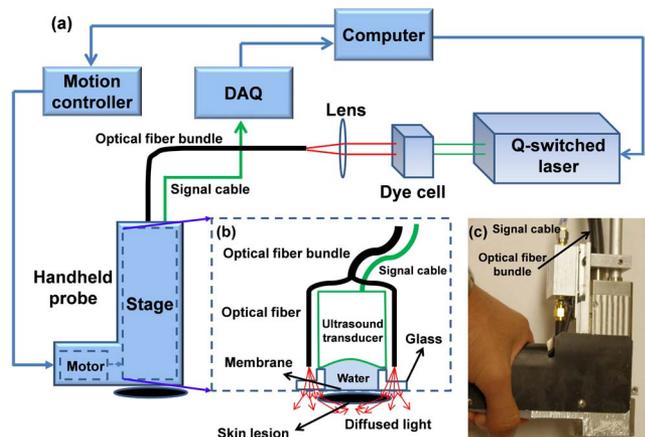

Fig. 1. Experimental handheld photoacoustic microscopy (PAM) system. (a) Schematic of the handheld PAM system. (b) Components held by the translation stage in the handheld probe. (c) Photograph of the handheld probe.

confinements, the PA signal is proportional to A_e. Thus, the PA signal in case 2 is 1660 times stronger than that in case 1. Because the light delivery is the only difference between the systems, their noise levels should be the same. Thus, the corresponding signal-to-noise ratio of the melanoma at the bottom boundary in the black-dashed-square area in case 2 is 1660 times greater than that in case 1. The results show that, with the new illumination mechanism, the bottom boundary of the melanoma can be much more sensitively detected.

We first used a human hair as a line target to measure the lateral resolution of this handheld PAM system. As shown in Fig. 3(a), the full width at half-maximum (FWHM) of the line spread function indicates a lateral resolution of 230 μm. Because of the large thickness of the hair (80 μm), the measured lateral resolution is slightly larger than the theoretical value ($0.72\lambda_0/\text{NA} = 173$ μm, where λ_0 is the center acoustic wavelength of the transducer) [28]. We next used a thin ink layer to measure the axial resolution. Taking the FWHM of the PA amplitude in the axial direction, we estimated the axial resolution as 59 μm [Fig. 3(b)], which is close to the theoretical value ($0.88v_s/\Delta f = 53$ μm, where v_s is the sound speed in soft tissue, and Δf is the frequency bandwidth of the transducer) [29].

Phantom experiments were conducted to demonstrate the ability of the handheld PAM system to measure deep melanomas. Three different diameters (7, 9.5, and 14 mm) of melanoma phantoms were prepared with varied thicknesses, shown in Figs. 4(a)–4(c). All the phantoms were made from a black ink and gelatin mixture, which had an absorption coefficient of 70 cm^{-1} at 650 nm, close to the real melanoma absorption coefficient. The background was made of a gelatin and intralipid mixture with a high scattering coefficient to mimic real tissue. As shown in Figs. 4(a)–4(c), our handheld system successfully detected both the top and bottom boundaries of all the melanoma phantoms. The maximum and minimum detected thicknesses of the phantoms were 0.7 and 4.1 mm, respectively. Thus, melanoma phantoms with all the T-classifications in the staging system have been measured. Figure 4(d) shows that our measured thicknesses agreed well with the preset values. Thus, the handheld PAM system can image deeply seated melanoma phantoms with high accuracy.

We also imaged mice with melanoma to show the *in vivo* detection ability of the handheld PAM system. Here we focused only on imaging deep melanoma to show the advantage of the new PAM system over our previous system. Melanoma B16 cells were subcutaneously injected into a nude mouse on the dorsal side
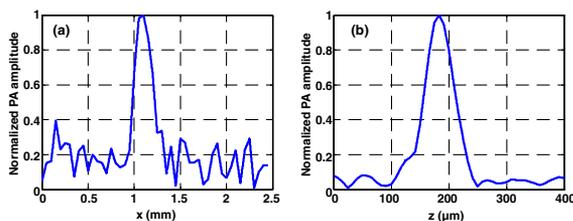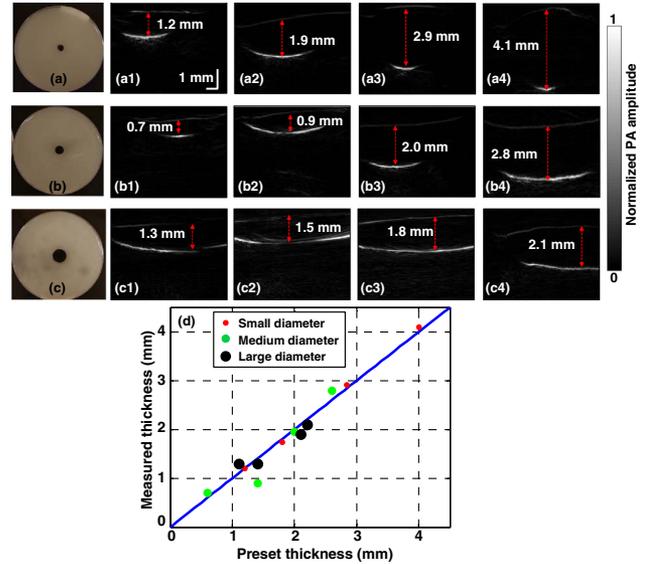

Fig. 4. Handheld PAM of melanoma phantoms. Photos of melanoma phantoms with different diameters [(a) 7 mm, (b) 9.5 mm, and (c) 14 mm]. (a1)–(a4), (b1)–(b4), and (c1)–(c4): PAM images of different thicknesses of melanoma phantoms with the same diameter as in (a), (b), and (c), respectively. (d) Measured thicknesses of melanoma phantoms versus preset thicknesses.

(Hsd:Athymic Nude-Foxn1NU, Harlan Co.; body weight: 20 g) to grow melanoma in the skin. All experimental animal procedures were carried out in conformity with the laboratory animal protocol approved by the School of Medicine Animal Studies Committee of Washington University in St. Louis. During image acquisition, the animal, warmed by an infrared lamp, was kept motionless using a breathing anesthesia system (E–Z Anesthesia, Euthanex). Figures 5(a) and 5(b) show that a melanoma with 3.66 mm thickness was imaged by our handheld system. Both the top and bottom boundaries of the melanoma and the skin surface can be clearly seen.
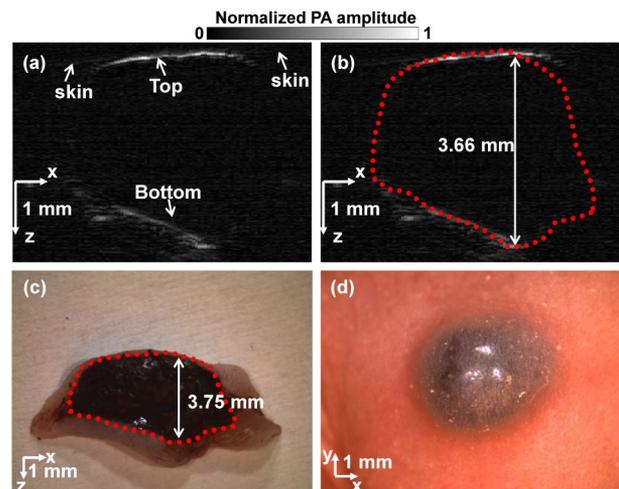

Fig. 5. Handheld PAM of melanoma in a nude mouse *in vivo*. (a) PAM image of the melanoma clearly showing both the top and bottom boundaries. (b) The same PAM image as (a). The red dots outline the melanoma according to the shape of the excised melanoma (red dots) in its photograph (c). Photograph of the melanoma taken *in vivo* (d).

Fig. 3. Spatial resolutions of the current PAM system. PA amplitudes in (a) the lateral x and (b) the axial z directions. The full widths at half-maximum are 230 μm in (a) and 59 μm in (b).

Shown in Fig. 5(c), the real thickness of the melanoma was measured to be 3.75 mm after excision, which is very close to our noninvasive measurement. A photograph of the melanoma *in vivo* is shown in Fig. 5(d). Therefore, the handheld PAM system can accurately detect the depth of deeply seated melanoma *in vivo*.

Compared to our previous PAM system for melanoma imaging, the new system can detect the depth of thicker melanomas by bypassing light around the tumor. In addition, a handheld design makes our new PAM system more suitable for clinical application. As shown in the phantom experiment, melanoma as thick as 4.1 mm can be detected, and in the *in vivo* experiment, melanoma with 3.75 mm thickness was imaged. Our measurements also show very high accuracy. As important, the improvement of the handheld system includes increasing the imaging speed. The current system employs a 10 Hz laser, which limits the imaging speed. Ten seconds is needed to scan a 10 mm length along the lateral direction with a step size of 100 μm. For clinical use, a rapid imaging system is always preferred, which can be achieved by using a pump laser with high pulse repetition rate (e.g., 1 kHz) [17]. We propose that the use of handheld PAM imaging, to aid in the determination of tumor depth, will facilitate the surgical treatment management of melanoma.

References

1. A. F. Jerant, J. T. Johnson, C. D. Sheridan, and T. J. Caffrey, Am. Fam. Physician **62**, 357 (2000).
2. E. M. Dunki-Jacobs, G. G. Callendar, and K. M. McMasters, Curr. Probl. Surg. **50**, 351 (2013).
3. American Cancer Society, http://www.cancer.org/acs/groups/content/@epidemiologysurveilance/documents/document/acspc-036845.pdf (2013).
4. K. M. Rubin, J. Dermatol. Nurses Assoc. **2**, 6 (2010).
5. L. Smith and S. MacNeil, Skin Res. Technol. **17**, 257 (2011).
6. P. Guitera and S. W. Menzies, Expert Rev. Anticancer Ther. **11**, 715 (2011).
7. I. H. Wolf, J. Smolle, H. P. Soyer, and H. Kerl, Melanoma Res. **8**, 425 (1998).
8. C. Benvenuto-Andrade, S. W. Dusza, A. L. C. Agero, A. Scope, M. Rajadhyaksha, A. C. Halpern, and A. A. Marghoob, Arch. Dermatol. **143**, 329 (2007).
9. M. A. Calin, S. V. Parasca, R. Savastru, M. R. Calin, and S. Dontu, J. Cancer Res. Clin. Oncol. **139**, 1083 (2013).
10. A. C. Halpern, Semin. Cutan. Med. Surg. **22**, 2 (2003).
11. T. Gambichler, P. Regeniter, F. G. Bechara, A. Orlikov, R. Vasa, G. Moussa, M. Stucker, P. Altmeyer, and K. Hoffmann, J. Am. Acad. Dermatol. **57**, 629 (2007).
12. S. Segura, S. Puig, C. Carrera, J. Palou, and J. Malvehy, J. Am. Acad. Dermatol. **61**, 216 (2009).
13. E. Dimitrow, M. Ziemer, M. J. Koehler, J. Norgauer, K. Konig, P. Elsner, and M. Kaatz, J. Invest. Dermatol. **129**, 1752 (2009).
14. W. Dummer, H. J. Blaheta, B. C. Bastian, T. Schenk, E. B. Brocher, and W. Remy, Arch. Dermatol. **131**, 279 (1995).
15. J. Bittoun, B. Querleux, and L. Darrasse, NMR Biomed. **19**, 723 (2006).
16. T. Z. Belhocine, A. M. Scott, E. Even-Sapir, J. L. Urbain, and R. Essner, J. Nucl. Med. **47**, 957 (2006).
17. Y. Zhou, J. J. Yao, and L. H. V. Wang, Opt. Lett. **38**, 2592 (2013).
18. L. H. V. Wang and S. Hu, Science **335**, 1458 (2012).
19. D. Razansky, C. Vinegoni, M. Distel, R. Ma, N. Perrimon, R. W. Koster, and V. Ntziachristos, Nat. Photonics **3**, 412 (2009).
20. Y. Zhou, J. Yao, K. I. Maslov, and L. V. Wang, J. Biomed. Opt. **19**, 37001 (2014).
21. J. T. Oh, M. L. Li, H. F. Zhang, K. Maslov, G. Stoica, and L. H. V. Wang, J. Biomed. Opt. **11**, 034032 (2006).
22. C. Kim, E. C. Cho, J. Chen, K. H. Song, L. Au, C. Favazza, Q. Zhang, C. M. Cobley, F. Gao, Y. Xia, and L. V. Wang, ACS Nano **4**, 4559 (2010).
23. H. F. Zhang, K. Maslov, G. Stoica, and L. V. Wang, Nat. Biotechnol. **24**, 848 (2006).
24. J. Staley, P. Grogan, A. K. Samadi, H. Cui, M. S. Cohen, and X. Yang, J. Biomed. Opt. **15**, 040510 (2010).
25. L. H. Wang, S. L. Jacques, and L. Q. Zheng, Comput. Methods Programs Biomed. **54**, 141 (1997).
26. S. L. Jacques and D. J. Mcauliffe, Photochem. Photobiol. **53**, 769 (1991).
27. L. V. Wang and H. Wu, *Biomedical Optics: Principles and Imaging* (Wiley, 2007).
28. E. W. Stein, K. Maslov, and L. H. V. Wang, J. Appl. Phys. **105**, 102027 (2009).
29. C. Zhang, Y. Zhou, C. Y. Li, and L. H. V. Wang, Appl. Phys. Lett. **102**, 163702 (2013).